Supporting Information

Popmintchev et al. 10.1073/pnas.0903748106

SI Text

Driving Light Source. The experimental data of Figs. 2–4 made use of IR laser source consisting of a 3-stage optical parametric amplifier (OPA) pumped by a high-energy Ti:Sapphire laser with pulse energies of 21 mJ and a pulse duration of 23 fs with a high-quality spatial profile of $M^2 < 1.2$, and at a repetition rate of 10 Hz. The OPA starts with a white light continuum seed, generated in a sapphire plate and then additionally chirped in time. In 3 subsequent amplification stages, the signal beam is further amplified in BBO crystals while isolating the idler beam in each of the subsequent steps. The tunability range of the OPA is 1.1–2.8 μm. Conversion efficiencies of 43% (total) were achieved for generating both signal and idler beams, with energy of up to 5.5 mJ in the signal beam at a wavelength of 1.3 μm. An output pulse duration of <35 fs (8 cycles at FWHM at 1.3 μm) was measured by using second-harmonic frequency resolved optical gating (SHG FROG).

Extreme High-Order Harmonic Source and X-ray Detection. The high harmonic beam is generated by focusing an intense driving laser pulse into a gas-filled hollow wave guide. The ratio of the waist of the laser beam to the wave guide radius (a = 125 or 200 μm) was ≈65%, ensuring guiding of the lowest loss EH_{11} mode. A continuous gas flow, with backing pressures of up to 6,000 torr, enters the wave guide through 2 laser-drilled holes. These holes effectively divide the wave guide into 3 sections. The end sections with relatively low gas throughput mitigate supersonic expansion of the high-pressure gas, which otherwise would lead to lower pressures in the interaction region. When steady state is established, the static gas pressure along the midsection has a negligible gradient, and pressure close to the backing pressure. A flat field X-ray spectrometer and a X-ray CCD are used to detect the generated harmonic beams. Depending on the photon energy range studied, various metal filters (Al, Zr, Ag, or Ti) are used to eliminate the fundamental laser light.

Scaling of Single Atom Yield at the Phase Matching Cutoff. The power scaling for the single atom yield at the phase matching cutoff $h\nu_{\mathrm{PM}}$ is calculated by using the strong field approximation (SFA) model, taking into account 8 classical trajectories (high-order electron returns). This model reproduced the $\lambda^{-5.5}$ single-atom effective nonlinear susceptibility scaling for a fixed photon energy interval and at constant laser intensity, as reported in refs. 1–3. Under the phase-matching conditions discussed, the predicted photon energies and laser intensities at $h\nu_{\mathrm{PM}}$ change as shown in Fig. 2*A* and Fig. S1*B*, and therefore, the scaling of the single-atom yield has to be revised. Using these parameters, the power law scaling of the HHG yield $P(\lambda_L)$, in a bandwidth ΔE, is calculated by using either the Fourier transform of the single atom dipole acceleration $a(\omega)$ or the dipole moment $d(\omega)$:

$$P_a(\lambda_L) = \int_{E-\Delta E/2}^{E+\Delta E/2} |a(\omega)|^2 \, d\omega \propto \lambda_L^x,$$

$$P_d(\lambda_L) = \int_{E-\Delta E/2}^{E+\Delta E/2} |d(\omega)|^2 \, d\omega \propto \lambda_L^y,$$

where x and y are presented in Table S1. Calculations were performed for a bandwidth corresponding to a single harmonic, or $\Delta E = 2E_f$, where E_f is the fundamental laser photon energy, and for a fixed fractional bandwidth of $\Delta E = E/100$, where E is the harmonic photon energy close to the phase matching cutoff.

The interchangeable prefactor $\omega_q^2|s_q|^2$, with $s_q = (1-\eta)d_q$, for the macroscopic HHG intensity dI_q in Eq. **3** emitted in a specific harmonic at the phase-matching cutoff $h\nu_{\mathrm{PM}}$, containing all of the wavelength scaling terms is given by: $\omega_q^2(\lambda_L)|d_q|^2 \propto \omega_q^{-2}(\lambda_L)|a_q|^2$. Here, $\omega_q(\lambda_L) \propto \lambda_L^{1.6-1.7}$ is the harmonic frequency at the phase matching-cutoff $h\nu_{\mathrm{PM}}$. Because the scaling of the critical ionization ($\eta_{CR} \propto \lambda_L^{-2}$) is almost independent of the gas species, the small variation of the power law scaling of $\omega_q(\lambda_L)$ is a consequence of the dependence of the ionization rate on the ionization potential of the gas (assuming ADK).

Phase-Matched HHG Using Loosely Focused Driving Laser Beam (No Wave Guiding). The predicted scaling of the critical ionization level and driving laser intensity is also applicable to HHG in a near-plane-wave propagation achieved by using a loosely focused laser beam. However, a larger laser energy is required in this case compared to HHG in a wave guide, because the laser beam cross-section increases. For a laser confocal parameter significantly longer than the interaction region, any geometric contribution to the phase mismatch can be neglected, giving:

$$\Delta k \approx \underbrace{-qp(1-\eta)\frac{2\pi}{\lambda_L}(\Delta\delta + n_2)}_{\text{atoms}} + \underbrace{qp\,\eta N_a r_e \lambda_L}_{\text{free electrons}}$$

To achieve phase matching, the ionization level must be close to the critical level η_{CR}. Thus, in contrast with a wave guiding geometry, where there is optimal phase-matching pressure, here, density of the medium is decoupled from the phase-matching process (this is also equivalent to a wave guide with a large inner diameter). In both cases, the density-length product of the nonlinear medium that optimizes the HHG emission near the phase-matching cutoff is set by the absorption cross-section of the generated X-rays: $\rho L_{\mathrm{med}} \approx 6\sigma_q^{-1}$ (from Eq. **3**). Therefore, the optimal pressure-length product and phase-matched HHG intensity are the same as the predicted in Fig. 5 *A–C*.

Evolution of the Driving Laser Field. The index of refraction and dispersion of He are relatively low. For example, the phase mismatch of neutral helium is equivalent to only a ≈500-μm-thick fused silica window under the considered conditions at $h\nu_{\mathrm{PM}}$ = 1 keV: 12 atm pressure and medium length >50 cm. Linear and nonlinear evolution of the laser field could limit the usable propagation length, however. In this context, we investigated competing limiting factors such as self-focusing, group velocity mismatch between the laser and the X-ray fields, ionization-induced laser energy loss, etc.

Nonlinear Effects. At high gas pressures, nonlinear distortion of the driving laser pulses might occur because of self-focusing or temporal or spectral modulation. Fortunately, this is not the case. The critical power for self-focusing in a wave guide is slightly higher than in the case for a bulk medium, and in general drops with increasing density of the medium: $P_{CR} \approx 1.86\lambda_L^2/(4\pi n_L p\tilde{n}_2)$, where n_L is the linear refractive index at λ_L (4). Because the optimal phase-matching pressure scales quadratically with laser wavelength, P_{CR} remains constant. On the other hand, the laser intensity required to generate a particular X-ray photon energy at $h\nu_{PM}$ decreases for longer-wavelength driving lasers. Therefore the laser power stays below the critical power for catastrophic nonlinear distortion. In the parameter range of interest, the dispersion term related to the nonlinear index of refraction n_2 is <2% of the linear refractive index term for He, Ne, and Ar at $\lambda_L = 0.8$ μm (5). This fraction decreases for mid-IR laser wavelengths. Hence, the Kerr nonlinear refractive index does not significantly modify the phase-matching conditions (Eq. **2**).

Plasma Frequency. Ionization Losses. Quantitatively, the free-electron density is $n_e \approx 10^{17}$ cm^{-3} for a fiber with a 250-μm diameter and drops for larger wave guide diameter. This corresponds to a plasma frequency cutoff wavelength more than ≈100 μm, well outside the region of interest for this work. Thus, even though the longer-wavelength laser beams will be more-sensitive to the plasma-created propagation distortions, the medium still remains underdense.

The ionization-induced laser energy loss is approximately equal to the energy acquired by the free electrons. An ionized electron gains a potential energy of I_p and a quiver energy that can be estimated both from experimental and theoretical above-threshold ionization (ATI) photoelectron spectra (1, 6, 7). ATI spectra exhibit a rapid decrease of photoelectron emission up to electron energies of $2U_p$, followed by a plateau region extending to ≈10 U_p. Using this photoelectron distribution, we estimate that the laser energy loss in He at $\lambda_L = 3$ μm for phase matching in the 1-keV region is 0.03 mJ/cm, corresponding to a 3% loss of the required laser energy per absorption length (e.g., $L_{abs} = 8.7$ cm for $a = 125$ μm and laser energy of ≈8.8 mJ in an 80-fs pulse duration). Use of a pressure gradient in combination with tapered wave guides may be used to maintain a high peak intensity and optimal phase-matching conditions over many-centimeters distances, despite ionization losses (8). In the case of HHG using a loosely focused driving laser beam, a slightly converging beam can be used instead. Also, to some extent the increase in ionization-induced laser energy loss at high photon energies is mitigated because the strong-field ionization considered here lies well within the tunneling-ionization regime. In other words, multiphoton ionization is suppressed, and most of the photoelectrons concentrate in a spike-like distribution at energies much less than $2U_p$. Moreover, the ratio of the yield of photoelectrons with kinetic energy $>2U_p$ compared with $<2U_p$ will drop more rapidly than the predicted scaling $\lambda_L^{-4.4}$ (6) when assuming constant laser intensity (under phase-matching conditions I_L decreases as shown in Fig. S1*B*).

Group Velocity Mismatch. The group velocity of the driving laser is given by $v_{gL} = c(n_L - \lambda_L dn_L/d\lambda)^{-1}$, where the index of refraction n_L at the laser wavelength is:

$$n_L \approx 1 + p(1-\eta)[\delta(\lambda_L) + \tilde{n}_2 I_L] - \frac{p\eta N_a r_e \lambda_L^2}{2\pi} - \frac{u_{11}^2 \lambda_L^2}{8\pi^2 a^2}$$

Under phase-matching conditions $n_L \to 1$. In contrast to phase velocity matching, group velocity matching $v_{gL} = c$ cannot be achieved because for a medium with normal dispersion, all of the terms in $dn_L/d\lambda$ have the same sign:

$$\frac{1}{v_{gL}} - \frac{1}{c} = -\frac{\lambda_L}{c}\frac{dn_L}{d\lambda}\bigg|_{\lambda_L} \approx$$

$$\approx \frac{\lambda_L}{c}\left(-p(1-\eta)\frac{d\delta(\lambda_L)}{d\lambda}\bigg|_{\lambda_L} + \frac{p\eta N_a r_e \lambda_L}{\pi} + \frac{u_{11}^2 \lambda_L}{4\pi^2 a^2}\right).$$

Hence, the group velocity of the driving laser is always less than the group velocity of the X-rays. Using wave guides with larger radius (a) minimizes $dn_L/d\lambda$ because it scales approximately as a^{-2} at the phase-matching cutoff. This increases the group velocity walk-off length (L_{GV}) between the driving pulse and an X-ray pulse (corresponding to a temporal walk-off of a laser pulse duration τ_{FWHM}, $L_{GV} = \tau_{FWHM}\,(1/v_{gL} - 1/c)^{-1}$. However, increasing the wave guide radius does not lead to a larger ratio of L_{GV}/L_{abs}, as would be required to obtain the best HHG flux (see Eq. **3**), because both lengths scale effectively as $\propto a^2$. Thus, the quadratic growth region for HHG emission is effectively limited to characteristic lengths comparable with L_{GV} (decreasing from ≈10 cm to ≈1 cm for driving laser wavelengths from 0.8 to 10 μm). The HHG signal still continues to increase for lengths $>L_{GV}$, but more slowly than a quadratic dependence. These walk-off effects can likely be ameliorated, however, by using tapered wave guides (8) with pressure ramps combined with shaping and/or lengthening the driving laser pulse. Specifically, the objective is to keep the point, at which the pulse intensity reaches that required to generate the target harmonic, moving at c. For medium lengths $>L_{GV}$, temporal reshaping of the envelope of the X-ray bursts will occur, together with the generation of longer trains of X-ray pulses.

Ponderomotive Effects. As the analysis shows, phase-matched HHG emission using mid-IR driving lasers scales well into the multi-keV regime while still requiring nonrelativistic laser intensities of 10^{14} to 10^{15} W/cm^2 (Fig. S1*B*). In contrast, when using a 0.8-μm driving laser, intensities $>10^{16}$ W/cm^2 are required for non-phase-matched harmonic emission in the keV region of the spectrum. At laser intensities of $I_L = 5 \times 10^{16}$ W/cm^2, the magnetic component $\boldsymbol{B}_L$ of the laser electromagnetic field can no longer be neglected, and the associated ponderomotive Lorentz force $\boldsymbol{F} = e(\boldsymbol{E}_L + v_e \mathrm{x} \boldsymbol{B}_L)$ induces a drift of the returning electron wave packet along the direction of laser propagation, away from the parent ion. Therefore, even if the phase mismatch is partially compensated, the decrease in recombination probability represents a fundamental limit for efficient single-atom HHG (9).

Using mid-IR driving wavelengths, however, the same cycle-averaged kinetic energy of the recolliding electron, U_p, corresponding to the same energy harmonics, is achieved by using a lower peak electric field that drops as $E_L \propto \lambda_L^{-1}$. Hence, the magnetic field is proportionally smaller. For the laser parameters required for phase matching up to $\lambda_L = 10$ μm (shown in Fig. S1*B*), the relativistic field strength parameter $\xi = eE_L\lambda_L/(2\pi m_e c^2)$, measuring the ratio between the amplitude of the speed of the quivering classical electron in E field, and the speed of light (10, 11), is <15% (Fig. S3*A*). Thus, the electron remains nonrelativistic. However, the magnetic field component of the ponderomotive force cannot be neglected because the excursion time for the recolliding electron is also increasing with longer wavelengths. The drift of the center of mass of the returning electron wave packet, $d \approx c\xi^2/(2\omega_L) \propto \lambda_L^3 E_L^2$, in the direction of laser propagation, starts to exceed the transverse wave packet spread (see Fig. S3*B*), $\Delta_z \approx 2^{3/4}(eE_L\hbar)^{1/2}/(\omega_L m_e^{3/4} I_p^{1/4})$ (9–11), for laser wavelengths longer than ≈5.9 μm in He, and ≈7 μm in Ne [points (1) and (2) in Fig. S3*C*]. Above these laser wavelengths, corresponding to full phase-matching cutoffs of ≈3 keV [point (1) and (2) in Fig. 2*A*], the recombination probability, and thus single-atom HHG efficiency, will decrease more rapidly than the drop associated with the 3D spread of the electron wave packet. External light fields can mitigate this effect (10–12). The practical upper limit for mid-IR phase-matched HHG emission can be more precisely determined through further single-atom calculations that take into account magnetic dipole and electric quadrupole interactions.

1. Tate J, et al. (2007) Scaling of wave-packet dynamics in an intense midinfrared field. *Phys Rev Lett* 98:013901.
2. Schiessl K, Ishikawa KL, Persson E, Burgdorfer J (2008) Wavelength dependence of high-harmonic generation from ultrashort pulses. *J Mod Opt* 55:2617–2630.
3. Frolov MV, Manakov NL, Starace AF (2008) Wavelength scaling of high-harmonic yield: Threshold phenomena and bound state symmetry dependence. *Phys Rev Lett* 100:173001.
4. Fibich G, Gaeta AL (2000) Critical power for self-focusing in bulk media and in hollow waveguides. *Opt Lett* 25:335–337.
5. Lehmeier HJ, Leupacher W, Penzkofer A (1985) Nonresonant 3rd order hyperpolarizability of rare-gases and N2 determined by 3rd harmonic-generation. *Opt Commun* 56:67–72.
6. Colosimo P, et al. (2008) Scaling strong-field interactions towards the classical limit. *Nat Phys* 4:386–389.
7. Blaga CI, et al. (2009) Strong-field photoionization revisited. *Nat Phys* 10.1038/nphys1228.
8. Christov IP, Kapteyn HC, Murnane MM (1998) Dispersion-controlled hollow core fiber for phase matched harmonic generation. *Opt Express* 3:360–365.
9. Walser MW, Keitel CH, Scrinzi A, Brabec T (2000) High harmonic generation beyond the electric dipole approximation. *Phys Rev Lett* 85:5082–5085.
10. Salamin YI, Hu SX, Hatsagortsyan KZ, Keitel CH (2006) Relativistic high-power laser–matter interactions. *Phys Rep* 427:41–155.
11. Hatsagortsyan KZ, Klaiber M, Müller C, Kohler MC, Keitel CH (2008) Laser-driven relativistic recollisions. *J Opt Soc Am B* 25:B92–B103.
12. Klaiber M, Hatsagortsyan KZ, Müller C, Keitel CH (2008) Coherent hard X rays from attosecond pulse train-assisted harmonic generation. *Opt Lett* 33:411–413.
13. Durfee CG, et al. (1999) Phase matching of high-order harmonics in hollow waveguides. *Phys Rev Lett* 83:2187–2190.
14. Durfee CG, et al. (1999) Guided-wave phase-matching of ultrashort-pulse light. *J Nonlinear Opt Phys Mater* 8:211–234.

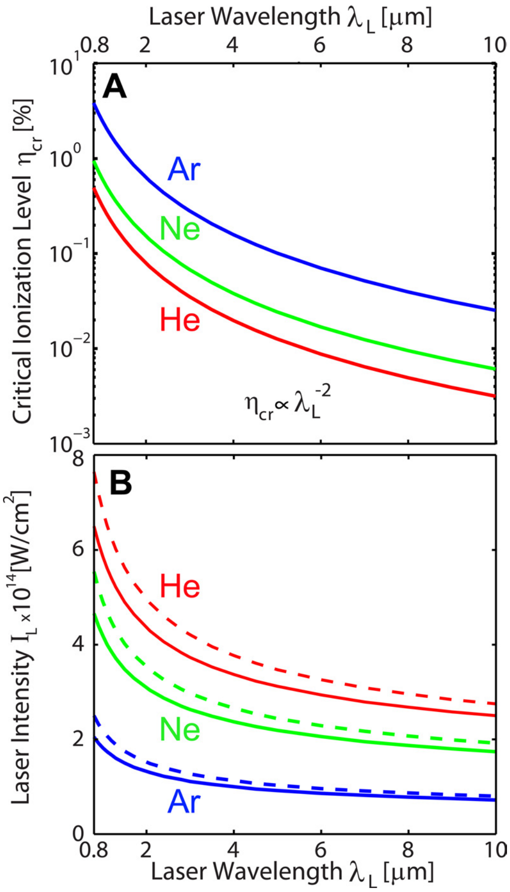

Fig. S1. (*A*) Critical ionization level above which full phase matching is not possible, which scales approximately as $\eta_{CR} \propto \lambda_L^{-2}$. (*B*) Predicted laser intensity required to reach the critical ionization level at the peak of the laser pulse on axis (solid line), and when modal averaging (13, 14) is taken into account (dashed line).

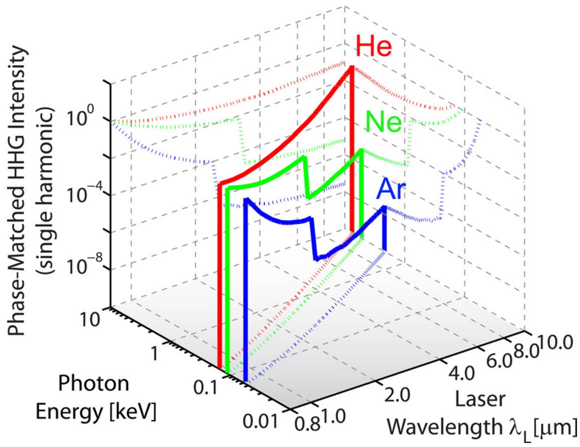

Fig. S2. Absorption-limited intensity of the phase-matched HHG in a bandwidth corresponding to a single harmonic at the phase-matching cutoffs for laser wavelengths between 0.8 and 10.0 μm. The curves are normalized to the phase-matched HHG emission at $\lambda_L = 0.8\ \mu$m. For high photon energies, group velocity mismatch and magnetic field effects would be expected to reduce the HHG flux below these predictions (see *Scaling of Phase Matching to keV Photon Energies* and *SI Text* for details).

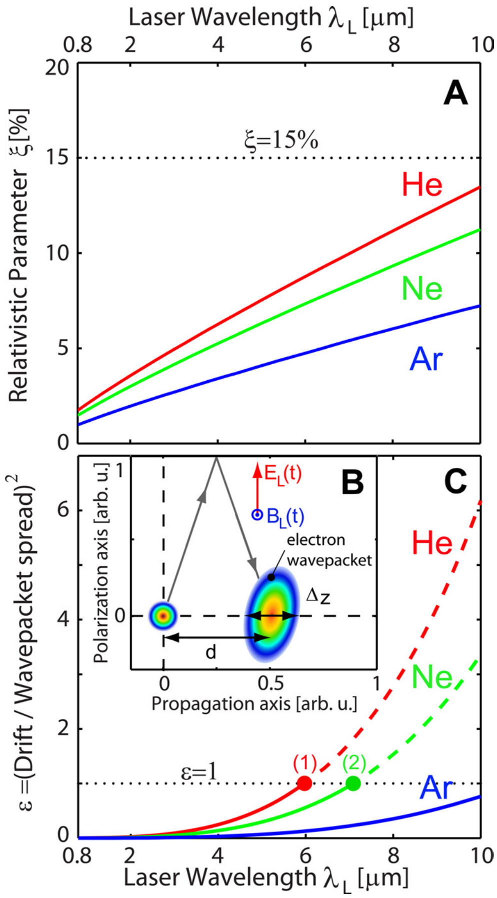

Fig. S3. (*A*) Ratio, ξ, of the velocity amplitude of the quivering electron in the laser field and the speed of light versus λ_L, showing that relativistic effects do not play a significant role under the conditions considered here. (*B*) Schematic of the drift of the electron wave packet due to the magnetic component of the laser field, along the propagation direction away from the nucleus (0, 0). (*C*) Squared ratio, ε, of the drift of the wave packet and its spread versus λ_L, showing that magnetic field effects may decrease the HHG flux only for λ_L approaching 6 μm in He and 7 μm in Ne.

Table S1. Power dependence of the single-atom yield with laser wavelength at the phase-matching cutoffs $h\nu_{PM}$

Gas	x*	x	y†	y
	$\Delta E = 2E_f$ ‡	$\Delta E = E/100$§	$\Delta E = 2E_f$	$\Delta E = E/100$
Helium	−9.00	−6.43	−14.05	−11.45
Neon	−8.62	−6.44	−13.44	−11.26
Argon	−8.38	−6.45	−12.57	−11.17

*Power dependence of the dipole acceleration $P_a \propto \lambda_L^x$.
†Power dependence of the dipole moment $P_d \propto \lambda_L^y$.
‡E_f—fundamental laser photon energy.
§E—harmonic photon energy close to the phase-matching cutoff.